PHYSICAL REVIEW B **108**, 125428 (2023)

Unveiling the hidden charge density wave spectral signature in $2H$-NbSe$_2$

Eunseok Oh,[1,2] Kyung-Hwan Jin,[1,*] and Han Woong Yeom[1,2,†]
[1]*Center for Artificial Low Dimensional Electronic Systems, Institute for Basic Science, Pohang 37673, Republic of Korea*
[2]*Department of Physics, Pohang University of Science and Technology, Pohang 37673, Republic of Korea*

(Received 9 June 2023; revised 1 September 2023; accepted 8 September 2023; published 21 September 2023)

Although $2H$-NbSe$_2$ has been discussed as a prototypical charge density wave (CDW) material with strong electron-phonon coupling, its energy gap structure, such as its position and size, has been elusive in spectroscopic measurements. We carefully reinvestigate the spectral change in the scanning tunneling microscopy and spectroscopy (STM/STS) when crossing the CDW transition in temperature and space. In contradiction to previous assignments, our spectroscopy measurements exhibit no significant spectral change across the CDW transition. Density functional theory calculations attribute the absence of the spectral signature to the CDW gap opening at the M point and the Γ-point-sensitive tunneling in the STS measurement. As an alternative CDW signature, we identify a strong bias-dependent modulation of local charge density across the Fermi energy which originates from the bonding/antibonding character of bands involved in the CDW gap at the M point. Our findings provide important insights for understanding partially gapped mutliband CDW materials.

DOI: 10.1103/PhysRevB.108.125428

I. INTRODUCTION

The emergence of energy gaps in electronic spectral functions is the major indication of the emergence of many-body insulating states such as Mott insulators [1], charge-density waves (CDWs) [2], and superconductivity [3] in interacting electronic systems. The spectroscopic characterization of energy gap structures is thus crucial for identifying and further understanding such many-body ground states of solids, especially when a few different degrees of freedom compete and/or collaborate for emerging phases. CDW phenomena, in which periodic modulations of charges and lattices emerge together, are classical but still intriguing examples in terms of energy gap structures and their origins. Although the CDW mechanism can be explained by the Peierls instability and Jahn-Teller distortion with moderate and strong electron-lattice interactions, respectively, in one-dimensional (1D) systems, the situation becomes more complex in higher dimensions where the Peierls instability is not significant. Instead, strong momentum-dependent electron-lattice interaction has been proposed as the major driving force [4–6], which can also involve other types of interactions such as strong electron correlation [7], charge ordering [8,9], excitonic interaction [10–12], and more.

One direct consequence of the complexity of CDWs in higher dimensions can be the complicated energy gap structure. Many multiband CDW materials show a lack of a global insulating energy gap, where only certain parts of energy bands in specific points of momentum space are observed to be gapped. One prototypical example is $2H$-NbSe$_2$, which has been studied widely as a model system for CDW and the interplay between charge order and superconductivity. It undergoes a CDW phase transition at 33 K with a very weak resistivity anomaly [13,14] and a superconducting phase transition at 7.2 K [15,16]. While theoretical studies based on density functional theory (DFT) calculations attributed the CDW transition to strong momentum-dependent electron-phonon coupling [5,17,18], the position and magnitude of the spectral gap in experiments have been elusive for decades. In momentum-resolved measurements of angle-resolved photoelectron spectroscopy (ARPES), the maximum gap size was estimated to be less than 8 meV from the Fermi energy [19,20]. What is intriguing in these data is that the energy gap structure around the Fermi energy remains consistent even at temperatures well above the CDW transition temperature T_C. Even with an improved momentum resolution, it is not clear whether the energy gap really changes at T_C [21]. This observation is inconsistent with the predictions of DFT calculations and was suggested to indicate a high-temperature pseudogap phase of uncertain origin [21].

The situation is even more unclear for the scanning tunneling spectroscopy (STS) measurements. A few early STS measurements suggested a rather symmetric gaplike feature with its edges at ±35 meV ($2\Delta_{\text{gap}}$ of 70 meV) [22,23], which is totally inconsistent with the ARPES data. A subsequent STS measurement suggested a much narrower asymmetric gap [24,25], but a very recent STS study on $2H$-Ta$_x$Nb$_{1-x}$Se$_2$ indicated that the inelastic electron tunneling process is the origin of these spectral features near the Fermi energy [26]. Namely, there is no consensus on the existence and size of a gap feature in STS at present. Alternatively, the change in topographic CDW modulation depending on biases was analyzed to capture the signature of CDW gap opening, which suggested the existence of an additional CDW gap well away from the Fermi energy [18,27–30]. On the other hand, the CDW state of $2H$-NbSe$_2$ was recently found to consist of two topologically intertwined structures [31] whose energy gap structures may be different, causing a laterally varying

---

[*] khwanjin@ibs.re.kr

[†] yeom@postech.ac.kr

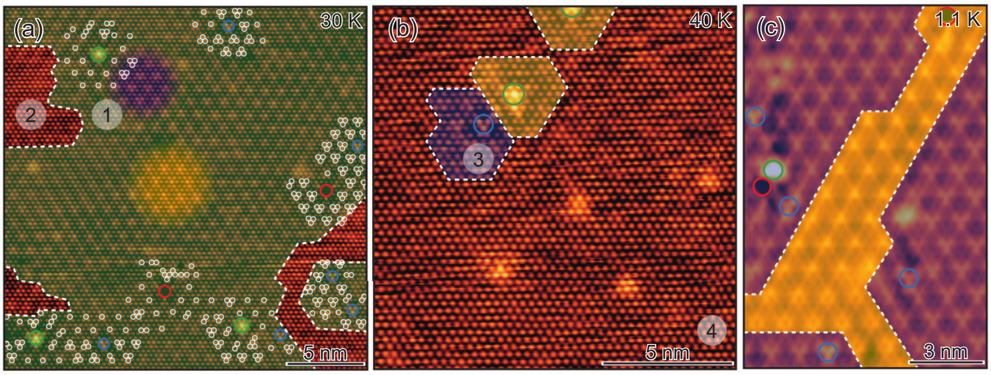

FIG. 1. STM topographic images ($V_{\mathrm{bias}} = 100$ mV, $I_{\mathrm{t}} = 500$ pA) at three representative temperatures: (a) 30 K (24 nm^2), (b) 40 K (14 nm^2), and (c) 1.1 K (10×15 nm^2). Colored shaded regions are CDW regions (HC: purple, AC: yellow, mixed: green), and examples of two well-defined CDW regions are colored in (a). The regions labeled 1 and 3 (2 and 4) indicate areas where CDW is locally present (absent). White dashed lines denotes phase boundaries. Colored circles indicate point defect sites. Especially, white circles denote protrusion spots, except for protrusions from other defects within eight atoms from the center position of a particular defect in (a).

gap. Therefore, to resolve the elusive CDW gap feature and discrepancies between STS, ARPES, and DFT results for $2H$-NbSe$_2$, a more systematic higher-resolution microscopic analysis is required together with extensive DFT calculations.

Here, we directly compare high-resolution dI/dV STS spectra and their numerical differentiation d^2I/dV^2 between normal and CDW regions below (30 K) and above (40 K) the transition temperature, respectively. Our STS results show no significant spectral changes when crossing the transition temperature and laterally traversing the normal and CDW regions. Additionally, we observe inelastic tunneling features in STS that are consistent with a recent report [26], but they do not exhibit any noticeable difference between the CDW and normal phases. These findings suggest the need for further theoretical and experimental investigations of the energy gap structure and the underlying mechanisms of the CDW transition in the $2H$-NbSe$_2$ material across its entire temperature range. Furthermore, investigation of the microscopic details of the phase of the CDW around the Fermi energy reveals a hidden local phase shift which is related to the orbital characteristics of the CDW-related bands. The calculated momentum-resolved density of states suggests that the CDW gap signature from the M point could be related to the momentum selectivity of the STS measurement. These findings provide insights into understanding CDW phenomena in two-dimensional (2D) multiband systems.

II. METHODS

$2H$-NbSe$_2$ single crystals were cleaved in high vacuum and transferred directly to an ultrahigh-vacuum chamber equipped with a commercial low-temperature scanning tunneling microscope. Pt/Ir tips were used for scanning tunneling microscopy (STM) measurements in constant-current mode at various temperatures (1.1, 4.3, 30, and 40 K). When we obtained dI/dV spectra with STM, the conventional lock-in technique was used with a modulation frequency of 1 kHz and an amplitude between 0.05 and 1 mV. Our DFT calculations were carried out using the Vienna Ab initio Simulation Package at the level of the generalized gradient approximation [32,33]. We used the projector augmented wave method for the description of the core-valence interaction. All the calculations were performed using a kinetic energy cutoff of 500 eV and a Monkhorst-Pack k-point grid of $7 \times 7 \times 1$ for the atomic relaxation and of $38 \times 38 \times 1$ for the electronic structure calculation for 3×3 CDW $2H$-NbSe$_2$. We used Methfessel-Paxton smearing with a smearing value of 0.1 eV. All structures were fully optimized until residual forces were less than 0.01 eV/Å. The spin-orbit coupling was included in the self-consistent electronic structure calculation. The calculated lattice constant is $a = 3.481$ Å, in agreement with experimental value. A vacuum space of 20 Å was employed to ensure decoupling between neighboring layers.

III. RESULTS AND DISCUSSION

We first compare temperature-dependent topographic measurements below (1.1 and 30 K) and above (40 K) T_{C}. Figures 1(a) and 1(b) are the empty-state STM topographies at 30 and 40 K. Below T_{C}, two distinct CDW structures can be observed in STM images [31]. These structures are characterized by a single protrusion and a trimer protrusion within a unit cell and are known as the anion-centered (AC) and hollow-centered (HC) structures, respectively [31]. In contrast, above T_{C} [Fig. 1(b)], only small areas near certain defects exhibit noticeable CDW modulations [27,34]. While HC and AC CDW domains are well defined with rather clear boundaries at a much lower temperature of 1.1 K [Fig. 1(c)], the phase landscape is more complicated at 30 K close to T_{C}. That is, in most of the area (about 90%), one of the two CDW structures is observed to develop [green region in Fig. 1(a)], but minor regions without clear CDW modulations (red regions) also exist. In addition, irregular protrusions that are neither single nor timer protrusions are also observed near defects (see the white circles near defects which denote the local protrusions). The origin of this defect-induced perturbation below T_{C} is not clear at present. However, the topographic evolution upon cooling, the expansion of ordered CDW areas, fits overall with the CDW transition picture discussed so far and is consistent with previous STM studies.

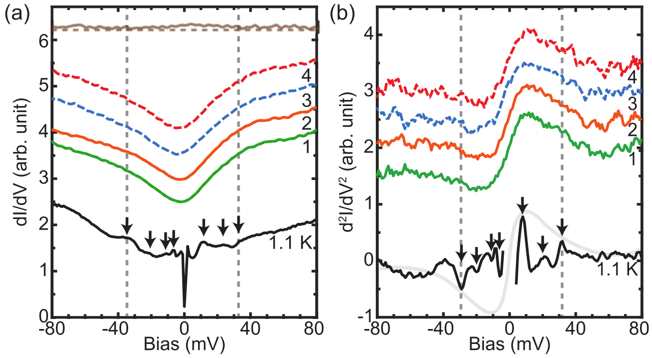

FIG. 2. Tunneling spectra across the CDW transition temperature. (a) Point dI/dV curves at different sites for various temperatures. The brown line denotes the difference between curves 1 and 4 with a reference line of zero. (b) d^2I/dV^2 curves from numerical differentiation of (a). Black arrows denote the step (peak) positions which were previously reported [26]. Numbers 1–4 indicate the spots represented in Figs. 1(a) and 1(b). The spectral curves above (below) T_C are indicated by the dashed (solid) lines. Dashed vertical gray lines are guides to the eye at selected energies (±35 mV) among the positions of the black arrows. The light gray line represents a guideline considering thermal broadening.

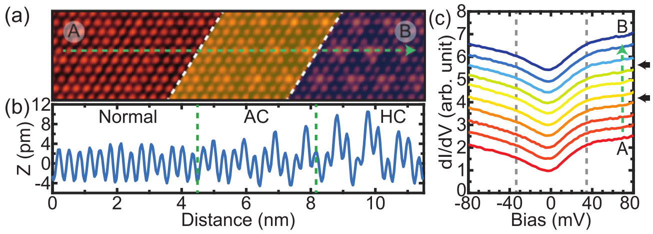

FIG. 3. Tunneling spectra across the structural dependence ($T = 30$ K, $V_{\mathrm{bias}} = 100$ mV). (a) Normal to CDW state regions containing all possible structure types (normal, HC, and AC) at 30 K. Dotted white lines are set at phase boundaries. Colored masks are covered at different CDW regions. (b) Corresponding height line profile of the green arrow from A to B. Corresponding phase boundary lines are set. Zero height is coordinated as an average height of the normal phase region. (c) Point dI/dV curves at equal distance intervals of the line from A to B in (a). Dashed vertical gray lines are guides to the eye at energies which show a gap-edge-like feature. Offsets are applied for clarity. Black arrows denote the locations of phase boundaries in (a).

To search the CDW energy gap, we measure the local tunneling dI/dV spectra [Fig. 2(a)] in the energy range of interest (±80 mV around the Fermi energy) at three representative temperatures for the areas with clear and no CDW modulations [Figs. 1(a)–1(c)]. The spectra at 1.1 K exhibit the superconducting gap at the Fermi energy with an energy scale of a few meV and a few fine modulations between +40 and −40 mV. The steps or peaks at ±35 and ±10 meV are particularly noticeable, and they were previously related to the CDW gap [22–25]. However, the complicated spectral structure with steps and peaks (black arrows) within this energy range (±40 mV) obviously indicates that the origin is not simply a CDW energy gap. Indeed, the derivative of this spectrum [Fig. 2(b)], which is normally proportional to the change in the density of states in elastic tunneling, shows a few step and peak structures in roughly symmetrical energy positions around the Fermi energy (indicated by arrows), consistent with a previous report [26] (see also Fig. S1 in the Supplemental Material [35]). These features can be interpreted as being due to the inelastic tunneling involving phonons. Namely, any clear sign of a CDW energy gap is missing in the low-temperature data.

We then try to find any possible change in the spectra upon the loss of the apparent CDW amplitude in STM at higher temperature. At 30 K, we find the broad diplike structure within ±35 mV [the green spectrum in Fig. 2(a)] which was previously assigned to a CDW gap [22,23]. Note that the energy of the minimum density of states is located at the Fermi level, which is inconsistent with the previous STS result [24]. However, when thermal broadening is considered, the d^2I/dV^2 curves shown in Fig. 2(b) exhibit peak and dip structures that correspond well to the smeared shape of the observed inelastic signal at 1.1 K. This suggests strongly that the broad diplike structure at 30 K is not due to the CDW gap but to the inelastic tunneling signals. This argument can further be supported by the absence of the correlation between this structure and the CDW amplitude. As shown in Figs. 2(a) and 2(b), the step or peak structure and the dI/dV spectra themselves in this energy range show no noticeable difference between the areas with the fully developed CDW and without any signature of the CDW. We can additionally see that there is no obvious difference between the spectra taken at 30 and 40 K. Even in the two extreme cases of the CDW region at 30 K (region 1) and the normal state region at 40 K (region 4), the subtracted spectra carry only a featureless null background in the whole energy range [top brown line in Fig. 2(a)].

The absence of the CDW-induced spectral change is further corroborated by the spatial coexistence of the CDW and normal domains at 30 K. For example, the STM image in Fig. 3(a) shows a surface area where the normal phase changes to a narrow AC CDW domain and then to the HC domain. Here, the term "normal phase" refers to the area where only a very faint CDW signature is present, which is presumably due to the decayed neighboring AC/HC CDW amplitudes. Through the fast Fourier transform of the STM images for each region, we were able to confirm distinct CDW signatures in each region (see Fig. S2 in the Supplemental Material). The evolution of the CDW amplitude as well as the lateral phase change can be clearly visualized by the topographic line, as shown in Fig. 3(b). However, no difference is observed in the STS line scan in Fig. 3(c). This is consistent with the results for selected regions at different temperatures [Fig. 2(a)], denying the existence of a gap feature with $2\Delta_{\mathrm{gap}} = 70$ or 24 meV suggested in previous works [22–24].

In order to understand these STS data, we perform DFT calculations. Our STM experiments primarily focus on the electronic structure associated with the CDW features observed on the top layer of NbSe$_2$; we modeled the 3 × 3 CDW system using one to three layers. Figure 4(a) shows the calculated band structure at normal and CDW states in the single-layer model. In our DFT calculation, we consider the HC CDW structure, which is the lowest-energy ground state [31]. At the normal (pristine) state, there are two Nb

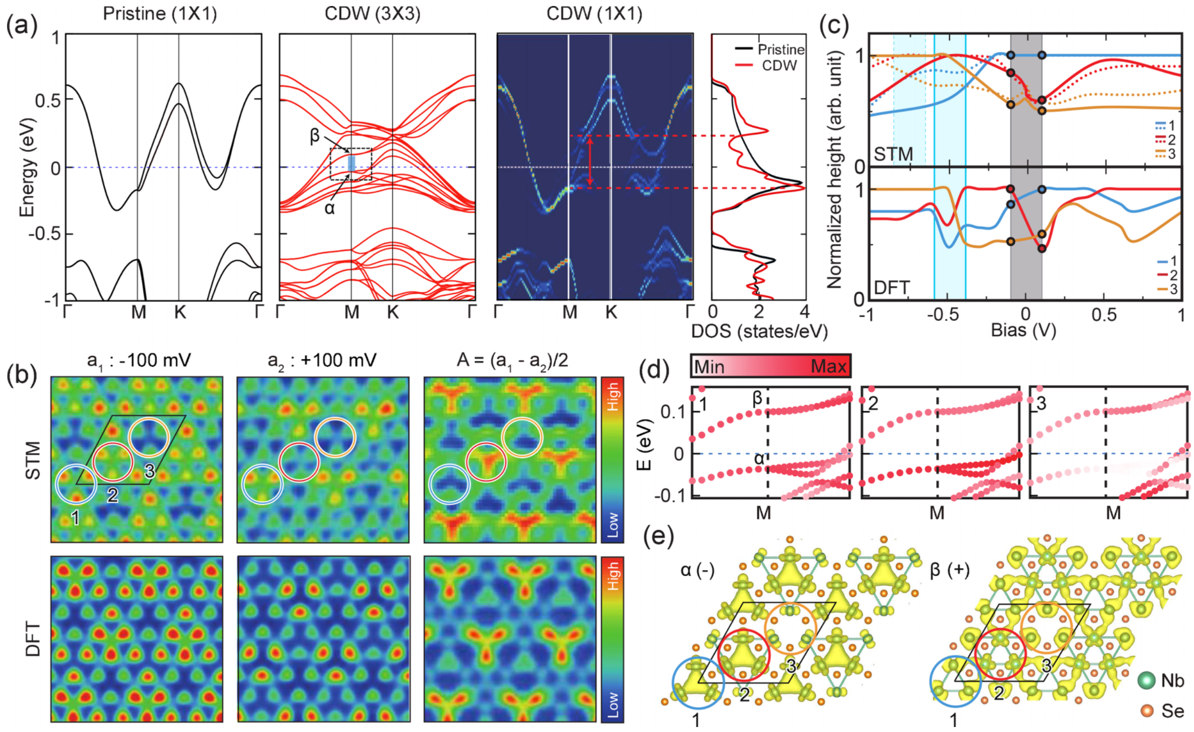

FIG. 4. Hidden phase shift from the CDW gap opening. (a) Left: The calculated band structure at a normal state in the 1 × 1 unit cell. Middle and right: The calculated band structures at the CDW state in the 3 × 3 supercell and the corresponding unfolded band structure in the Brillouin zone of the 1 × 1 unit cell. The blue square denotes the evolved CDW gap at the *M* point around the Fermi energy. The calculated DOSs are added for the normal and CDW phases. The red arrow represents the energy range where the DOS is modulated by the CDW. (b) Top: Bias-dependent STM topographic images for biases of opposite polarity [$V_{\text{bias}} = -100$ mV (first panel) and $+100$ mV (second panel), $I_t = 1$ nA, $T = 4.3$ K] in the HC CDW state and an antisymmetrized image (third panel) for both images. Bottom: Corresponding DFT simulated images. The black rhombus denotes a CDW 3 × 3 supercell. Se(Nb) trimer regions in the CDW state are grouped by colored circles (1, blue circle; 2, red circle; 3, yellow circle). (c) Normalized height value of protrusion centers of three types of Se trimers [colored circle regions in (b)] for a wide range of the bias voltage. Height values of each bias are normalized by the highest height value among the three types (1, 2, and 3). STM height results were obtained at intervals of 50 mV within the range of −200 to 200 mV, while data outside of this range were acquired at intervals of 200 mV. In the top panel, results obtained from different samples are distinguished by solid and dotted lines. Small colored circle are especially marked on graph from height values in (b). The gray and cyan shaded areas represent where the phase inversion occurs. (d) The projected band structures around the *M* point [dashed rectangle in (a)], where the color bar represents the contributions from Nb_1, Nb_2, and Nb_3 atoms, from left to right. (e) Partial charge densities of the occupied and unoccupied states, as indicated by α (−) and β (+) states in (a), respectively.

d bands crossing the Fermi energy along the *M*-*K* line [the first panel in Fig. 4(a)] [20,25]. At the CDW state, among several metallic bands crossing the Fermi energy, a significant CDW gap opens [blue square in the second panel in Fig. 4(a)] only around the *M* point in the bands closest to the Fermi energy, with a gap size of ∼120 meV, which is much larger than those suggested in previous experimental works [24,25]. The evolution of the gap opening upon increasing the CDW lattice distortion is detailed further in Figs. S3 and S4 in the Supplemental Material. Together with the main CDW gap at the *M* point, the metallic bands along the *M*-*K* direction undergo deformation during the CDW transition. In the unfolded band structure in the 1 × 1 Brillouin zone [third panel in Fig. 4(a)], a large gap along the *M*-*K* line, which matches the *K*-centered Fermi surface barrels in previous ARPES measurements [19,20], indicates the overall reduction in the DOS in a wide energy range of up to ∼0.4 eV in the CDW transition [red dashed guide lines between the third and fourth panels in Fig. 4(a)]. Note that the band structure of the AC CDW state shows a much smaller CDW gap compared to the HC CDW case (see Fig. S5 in the Supplemental Material).

We suggest that the absence of a CDW gap signature in dI/dV spectra must be related to the strong momentum-dependent tunneling in STS measurements. In the calculated DOS [Fig. 4(a)], the high density of states around the Fermi energy is remarkable, resulting from two Nb *d* metallic bands. However, the STS results show a weak dI/dV intensity near the Fermi level, while the overall peak positions [25,27,36] in the dI/dV spectra are in good agreement with the DFT results (see Fig. S6 in the Supplemental Material). This situation is also distinct from the ARPES measurements [19,20,25], which clearly reproduce a strong DOS intensity at ~ -0.2 eV below the Fermi energy. In order to reproduce such weak dI/dV signatures near the Fermi level, we adopt a Γ-point-weighted *k* mesh ($\sim e^{-\alpha k^2}$) in calculating the DOS since the tunneling process predominantly occurs about the Γ point. As the α value increases, the contribution of states near the *M* and *K* points decreases, leading to a significant reduction in the DOS near the Fermi level. The adjusted DOS successfully reproduces the low-energy dI/dV curve (see Fig. S6 in the Supplemental Material). This result indicates the CDW gap signature from the M point could be suppressed in the tunneling process.

One thus has to find another way to identify the CDW gap signature in STS measurements. Following a few previous works in this respect, we analyze bias-dependent topographic images of the HC CDW state. Figure 4(b) shows the corresponding STM topographic images at 4.3 K and the corresponding simulated images in selected biases. In the HC CDW structure [Fig. 4(e)], the Nb atoms in a 3 × 3 unit cell can be grouped into three different configurations [Nb_1, Nb_2, and Nb_3; black rhombus in Fig. 4(b)] through the formation of a hexamer and a trimer [31]. Each group of Nb atoms forms a Nb trimer (colored circles), which distorts top-layer Se trimers, which are responsible for STM topographic protrusions. In both filled and empty biases [first and second panels in the top row of Fig. 4(b)] strong Se trimer protrusions [group 1 (blue circle)] exist due to the contracted Nb trimer [18,31,34]. The brightness of the Se trimer in group 3 (yellow circle) is the weakest, and there is no significant difference above and below the Fermi level. Interestingly, the contrast of a Se trimer in group 2 (red circle) is significantly changed with a change in the bias polarity, which was not noticed in the previous analysis [18]. In the antisymmetrized image [third panel in the top row of Fig. 4(b)], we can see the strong contrast in these Se atoms. The corresponding simulated images reproduce well the contrast change in group 2 Se atoms [Fig. 4(b), bottom row] observed experimentally. Note that, in the bias energy range near the Fermi level, the states around the M and K points are naturally selected, which makes the STM simulation reflect the characteristics of wave functions around the M and K points. That is, the momentum-selective characteristic is implicitly incorporated into the STM simulations. The signature of the topographic contrast change can also be observed in the height profiles. The normalized height values of the protrusion centers of three groups of Se trimers are plotted in Fig. 4(c) in the full bias range (−1 to 1 V). The height values are normalized to the maximum of the measured STM images. In particular, CDW amplitude changes are distinctly shown across the Fermi energy (gray shaded area) in the Nb_2 trimer region discussed above [see small colored circles in Fig. 4(c)].

The above topographic contrast change is directly related to the CDW gap and the orbital characteristic of the bands involved. Figure 4(d) shows the contributions of Nb_1, Nb_2, and Nb_3 atoms to the bands around the M point. There is a clear contrast in the contributions of Nb_2 and Nb_3 atoms to the bottom conduction and top valence bands at the M point. However, for the Nb_1 atoms, the DOSs from the valence and conduction bands are almost the same, which explains the absence of the strong topographic contrast change in region 1 in the STM results. The partial charge density of occupied and unoccupied states [α (−) and β (+) states in Fig. 4(a)] at the M point more clearly shows the charge density modulation in three trimer regions due to the CDW [Fig. 4(e)]. Especially, Nb_2 (Nb_3) atoms exhibit a bonding (antibonding) character in the valence band, while showing the opposite trend in the conduction band. Note that the expected contrast change in region 3 seems to be suppressed in measurements due to the dominant density of states in regions 2 [Fig. 4(d)]. For the Nb_1 atoms, they undergo contraction, resulting in the formation of a small Nb trimer CDW structure, and the CDW bonding and antibonding states can be observed in the partial charge density [blue circles in Fig. 4(e)]. However, these bonding and antibonding states exert a nearly equal influence on the adjacent Se trimers in the top layer. In the Nb_1 trimer region, this is evident from the STM images, which show a relatively strong intensity and no variation above and below the Fermi level.

In a 2D CDW system forming the simplest 2 × 2 supercell [30,37], the global contrast inversion of STM images occurs around the CDW gap because the CDW unit cell is simply divided by two regions which have either bonding or antibonding character. On the other hand, in a 3 × 3 system, there are two distinct types of regions (Nb trimer/Nb hexamer) within the CDW unit cell that can exhibit bonding or antibonding character in each region, resulting in a more complex contrast variation within a CDW unit cell. In a more extended 2D CDW system such as the VTe_2 monolayer with a 4 × 4 CDW unit cell [38], the CDW contrast variations are even more complicated. It is also worth noting the origin of the CDW contrast inversion signature observed far below the Fermi level. As also shown in Fig. 4(c), the contrast inversion is also seen around −0.5 eV, which was considered to be the result of another CDW gap opening in the valence band [27,29]. In the analysis of the bias-dependent STM images, specifically two cases shown in Fig. 4(c), the contrast inversion occurs at two different energy positions (cyan shaded areas), −0.5 and −0.75 eV, which are consistent with the results of two previous studies [27,29]. We find that two distinct energy regions exists where the dominant band character is either Nb (>-0.4 eV) or Se (<-0.5 eV; see Fig. S7 in the Supplemental Material). Accordingly, the observed contrast inversion in the valence band around −0.5 eV can be attributed to the transition of the band character from Se to Nb, rather than the opening of a CDW gap.

IV. CONCLUSION

In summary, our results showed that the 2H-NbSe_2 system does not exhibit any gaplike feature or significant reduction in STS spectral weight near the Fermi level during the CDW transition despite the well-defined structural changes caused by the CDW transition. We suggested the Γ-point sensitivity of the tunneling reduces the CDW gap signature, which is located at the M point in the Brillouin zone. This indicates the need to reexamine the assignment of the CDW gap in the previous STS measurements. We found a local DOS contrast modulation across the Fermi energy, which is a trace of the CDW gap opening at the M point. This part of the results indicates that the charge modulation in a 2D CDW unit cell can be complicated and a simple CDW phase inversion does not necessarily occur.

ACKNOWLEDGMENTS

This work was supported by the Institute for Basic Science (Grant No. IBS-R014-D1). K.-H.J. is supported by the Institute for Basic Science (Grant No. IBS-R014-Y1).

[1] M. Imada, A. Fujimori, and Y. Tokura, Metal-insulator transitions, Rev. Mod. Phys. **70**, 1039 (1998).

[2] G. Grüner, The dynamics of charge-density waves, Rev. Mod. Phys. **60**, 1129 (1988).

[3] M. Tinkham, *Introduction to Superconductivity*, 2nd ed. (Dover, Mineola, NY, 2004).

[4] M. D. Johannes and I. I. Mazin, Fermi surface nesting and the origin of charge density waves in metals, Phys. Rev. B **77**, 165135 (2008).

[5] F. Weber, S. Rosenkranz, J.-P. Castellan, R. Osborn, R. Hott, R. Heid, K.-P. Bohnen, T. Egami, A. H. Said, and D. Reznik, Extended Phonon Collapse and the Origin of the Charge-Density Wave in 2H-NbSe$_2$, Phys. Rev. Lett. **107**, 107403 (2011).

[6] K. Wijayaratne, J. Zhao, C. Malliakas, D. Y. Chung, M. G. Kanatzidis, and U. Chatterjee, Spectroscopic signature of moment-dependent electron-phonon coupling in 2H-TaS$_2$, J. Mater. Chem. C **5**, 11310 (2017).

[7] D. Mou, A. Sapkota, H.-H. Kung, V. Krapivin, Y. Wu, A. Kreyssig, X. Zhou, A. I. Goldman, G. Blumberg, R. Flint, and A. Kaminski, Discovery of an Unconventional Charge Density Wave at the Surface of K$_{0.9}$Mo$_6$O$_{17}$, Phys. Rev. Lett. **116**, 196401 (2016).

[8] J. J. Yang, Y. J. Choi, Y. S. Oh, A. Hogan, Y. Horibe, K. Kim, B. I. Min, and S.-W. Cheong, Charge-Orbital Density Wave and Superconductivity in the Strong Spin-Orbit Coupled IrTe$_2$:Pd, Phys. Rev. Lett. **108**, 116402 (2012).

[9] Q. Wang, K. von Arx, M. Horio, D. J. Mukkattukavil, J. Küspert, Y. Sassa, T. Schmitt, A. Nag, S. Pyon, T. Takayama, H. Takagi, M. Garcia-Fernandez, K.-J. Zhou, and J. Chang, Charge order lock-in by electron-phonon coupling in La$_{1.675}$Eu$_{0.2}$Sr$_{0.125}$CuO$_4$, Sci. Adv. **7**, eabg7394 (2021).

[10] H. Cercellier, C. Monney, F. Clerc, C. Battaglia, L. Despont, M. G. Garnier, H. Beck, P. Aebi, L. Patthey, H. Berger, and L. Forró, Evidence for an Excitonic Insulator Phase in 1T-TiSe$_2$, Phys. Rev. Lett. **99**, 146403 (2007).

[11] A. Kogar, M. S. Rak, S. Vig, A. A. Husain, F. Flicker, Young I. Joe, L. Venema, G. J. MacDougall, T. C. Chiang, E. Fradkin, J. van Wezel, and P. Abbamonte, Signatures of exciton condensation in a transition metal dichalcogenide, Science **358**, 1314 (2017).

[12] C. Chen, B. Singh, H. Lin, and V. M. Pereira, Reproduction of the Charge Density Wave Phase Diagram in 1T-TiSe$_2$ Exposes Its Excitonic Character, Phys. Rev. Lett. **121**, 226602 (2018).

[13] D. E. Moncton, J. D. Axe, and F. J. DiSalvo, Study of Superlattice Formation in 2H-NbSe$_2$ and 2H-TaSe$_2$ by Neutron Scattering, Phys. Rev. Lett. **34**, 734 (1975).

[14] D. E. Moncton, J. D. Axe, and F. J. DiSalvo, Neutron scattering study of the charge-density wave transitions in 2H-TaSe$_2$ and 2H-NbSe$_2$, Phys. Rev. B **16**, 801 (1977).

[15] S. Foner and E. J. McNiff, Upper critical fields of layered superconducting NbSe$_2$ at low temperature, Phys. Lett. A **45**, 429 (1973).

[16] P. de Trey, S. Gygax, and J.-P. Jan, Anisotropy of the Ginzburg-Landau parameter κ in NbSe$_2$, J. Low Temp. Phys. **11**, 421 (1973).

[17] F. Flicker and J. van Wezel, Charge order from orbital-dependent coupling evidenced by NbSe$_2$, Nat. Commun. **6**, 7034 (2015).

[18] J. Dai, E. Calleja, J. Alldredge, X. Zhu, L. Li, W. Lu, Y. Sun, T. Wolf, H. Berger, and K. McElroy, Microscopic evidence for strong periodic lattice distortion in two-dimensional charge-density wave systems, Phys. Rev. B **89**, 165140 (2014).

[19] S. V. Borisenko, A. A. Kordyuk, V. B. Zabolotnyy, D. S. Inosov, D. Evtushinsky, B. Büchner, A. N. Yaresko, A. Varykhalov, R. Follath, W. Eberhardt, L. Patthey, and H. Berger, Two Energy Gaps and Fermi-Surface “Arcs” in NbSe$_2$, Phys. Rev. Lett. **102**, 166402 (2009).

[20] D. J. Rahn, S. Hellmann, M. Kalläne, C. Sohrt, T. K. Kim, L. Kipp, and K. Rossnagel, Gaps and kinks in the electronic structure of the superconductor 2H-NbSe$_2$ from angle-resolved photoemission at 1 K, Phys. Rev. B **85**, 224532 (2012).

[21] U. Chatterjee, J. Zhao, M. Iavarone, R. Di Capua, J. P. Castellan, G. Karapetrov, C. D. Malliakas, M. G. Kanatzidis, H. Claus, J. P. C. Ruff, F. Weber, J. van Wezel, J. C. Campuzano, R. Osborn, M. Randeria, N. Trivedi, M. R. Norman, and S. Rosenkranz, Emergence of coherence in the charge-density wave state of 2H-NbSe$_2$, Nat. Commun. **6**, 6313 (2015).

[22] C. Wang, B. Giambattista, C. G. Slough, R. V. Coleman, and M. A. Subramanian, Energy gaps measured by scanning tunneling microscopy, Phys. Rev. B **42**, 8890 (1990).

[23] H. F. Hess, R. B. Robinson, and J. V. Waszczak, STM spectroscopy of vortex cores and the flux lattice, Phys. B (Amsterdam, Neth.) **169**, 422 (1991).

[24] A. Soumyanarayanan, M. M. Yee, Y. He, J. van Wezel, D. J. Rahn, K. Rossnagel, E. W. Hudson, M. R. Norman, and J. E. Hoffman, Quantum phase transition from triangular to stripe charge order in NbSe$_2$, Proc. Natl. Acad. Sci. USA **110**, 1623 (2013).

[25] M. M. Ugeda, A. J. Bradley, Y. Zhang, S. Onishi, Y. Chen, W. Ruan, C. Ojeda-Aristizabal, H. Ryu, M. T. Edmonds, H.-Z. Tsai, A. Riss, S.-K. Mo, D. Lee, A. Zettl, Z. Hussain, Z.-X. Shen, and M. F. Crommie, Characterization of collective ground states in single-layer NbSe$_2$, Nat. Phys. **12**, 92 (2016).

[26] X.-Y. Hou, F. Zhang, X.-H. Tu, Y.-D. Gu, M.-D. Zhang, J. Gong, Y.-B. Tu, B.-T. Wang, W.-G. Lv, H.-M. Weng, Z.-A. Ren, G.-F. Chen, X.-D. Zhu, N. Hao, and L. Shan, Inelastic Electron Tunneling in 2H-Ta$_x$Nb$_{1-x}$Se$_2$ Evidenced by Scanning Tunneling Spectroscopy, Phys. Rev. Lett. **124**, 106403 (2020).

[27] C. J. Arguello, S. P. Chockalingam, E. P. Rosenthal, L. Zhao, C. Gutiérrez, J. H. Kang, W. C. Chung, R. M. Fernandes, S. Jia, A. J. Millis, R. J. Cava, and A. N. Pasupathy, Visualizing the charge density wave transition in 2H-NbSe$_2$ in real space, Phys. Rev. B **89**, 235115 (2014).

[28] Á. Pásztor, A. Scarfato, M. Spera, C. Barreteau, E. Giannini, and C. Renner, Holographic imaging of the complex charge density wave order parameter, Phys. Rev. Res. **1**, 033114 (2019).

[29] Á. Pásztor, A. Scarfato, M. Spera, F. Flicker, C. Barreteau, E. Giannini, J. van Wezel, and C. Renner, Multiband charge density wave exposed in a transition metal dichalcogenide, Nat. Commun. **12**, 6037 (2021).

[30] M. Spera, A. Scarfato, Á. Pásztor, E. Giannini, D. R. Bowler, and C. Renner, Insight into the Charge Density Wave Gap from Contrast Inversion in Topographic STM Images, Phys. Rev. Lett. **125**, 267603 (2020).

[31] G. Gye, E. Oh, and H. W. Yeom, Topological Landscape of Competing Charge Density Waves in 2H-NbSe$_2$, Phys. Rev. Lett. **122**, 016403 (2019).

[32] G. Kresse and J. Furthmüller, Efficient iterative schemes for *ab initio* total-energy calculations using

a plane-wave basis set, Phys. Rev. B **54**, 11169 (1996).

[33] J. P. Perdew, K. Burke, and M. Ernzerhof, Generalized Gradient Approximation Made Simple, Phys. Rev. Lett. **77**, 3865 (1996).

[34] E. Oh, G. Gye, and H. W. Yeom, Defect-Selective Charge-Density-Wave Condensation in $2H$-NbSe$_2$, Phys. Rev. Lett. **125**, 036804 (2020).

[35] See Supplemental Material at http://link.aps.org/supplemental/10.1103/PhysRevB.108.125428 for tunneling spectra at different temperatures; FFT analysis of extended images; the dependence of the band structure and DOS as a function of the lattice distortion; the band structure of the AC CDW phase; -point weight enhanced DOS; contrast inversion due to the Se bands.

[36] J. Silva-Guillén, P. Ordejón, F. Guinea, and E. Canadell, Electronic structure of $2H$-NbSe$_2$ single-layers in the CDW state, 2D Mater. **3**, 035028 (2016).

[37] P. Mallet, K. M. Zimmermann, Ph. Chevalier, J. Marcus, J. Y. Veuillen, and J. M. Gomez Rodriguez, Contrast reversal of the charge density wave STM image in purple potassium molybdenum bronze K$_{0.9}$Mo$_6$O$_{17}$, Phys. Rev. B **60**, 2122 (1999).

[38] G. Miao, S. Xue, B. Li, Z. Lin, B. Liu, X. Zhu, W. Wang, and J. Guo, Real-space investigation of the charge density wave in VTe$_2$ monolayer with broken rotational and mirror symmetries, Phys. Rev. B **101**, 035407 (2020).